Turbulence structure and the development of secondary outer-bank flow cells at multiple discharges in a meander bend

Hackney, C.R.[1] and Parsons, D.R.[2]

[1]School of Geography, Politics and Sociology, Newcastle University, Newcastle-upon-Tyne, UK, christopher.hackney@newcastle.ac.uk, twitter: @drchrishackney

[2]Energy and Environment Institute, University of Hull, Hull, UK, D.Parsons@hull.ac.uk, twitter: @bedform

This paper is not peer reviewed submitted to EarthArXiv, but has been submitted for consideration in *Earth Surface Processes and Landforms*

Abstract

The erosion of the outer-banks of meander bends is mediated by the form roughness of the bank topography, which has been shown to affect near bank three-dimension flow structures and shear stresses. As the scales of bank roughness is known to vary vertically from bank toe to bank edge variations in flow discharge are likely to driver changes in near-bank flow velocities and turbulent structures in the near-bank zone. However, to date field observations of three-dimensional flow in the near-bank zone across multiple discharges remain limited. Here, we report observations of three-dimensional flow characteristics in the near-bank zone of a meander bend at a range of discharge levels; low (9 m^3 s^{-1}), mid- (23 m^3 s^{-1}) and bankfull (90 m^3 s^{-1}). Our results reveal that the relationship between the presence of a secondary outer-bank flow cell (SOC) and magnitudes of turbulent kinetic energy (TKE) and shear stresses vary with discharge. At high flows, the presence of a SOC is related to increased TKE, whilst at mid-flow discharges SOCs are associated with reduced TKE compared to transects where SOCs are absent. At low flows there is no observed pattern between TKE and the presence/absence of a SOC. We attribute these patterns to the role that failed material at the bank toe plays in deflecting and modulating near-bank flows. This work highlights how important detailed flow data across multiple discharges is in terms of understanding flow through meander bends and thus the impact these flow processes will have on longer term bend morphodynamics.

Keywords

Bank erosion, flow structures, near-bank flow, turbulence

1. Introduction

Given that flows in natural channels are fully turbulent, it is expected that outer-bank erosion rates are also controlled to a large extent by turbulent stresses (Abad and Garcia, 2009a; Engel and Rhoads, 2017; Jamieson et al., 2010). The removal and remobilisation of bank sediment resulting from this interplay ultimately drives channel migration and results in the generation of classical meandering patters across many lowland alluvial rivers (Brice, 1974; Parker et al., 2011; Rinaldi and Darby, 2007). The erosion of the outer-banks of meander bends is mediated by the form roughness of the bank topography, which has been shown to affect near bank three-dimension flow structures and shear stresses (Hackney et al., 2015; Kean and Smith, 2006a, 2006b; Konsoer et al., 2016). As the scales of bank roughness is known to vary vertically from bank toe to bank edge (Konsoer et al., 2017), as flow levels vary across a hydrograph, the scales of roughness that actively impact on the near-bank flow velocities will change. There is, therefore, a dependence upon flow discharge with respect to the modulation of near-bank flow velocities and turbulent structures in the near-bank zone (NBZ: here defined as the region of flow from the bank edge to the bank toe; Figure 1) resulting from bank roughness that is not yet fully appreciated. Whilst previous research has highlighted the complex nature of outer-bank turbulence (Blanckaert, 2009; Blanckaert et al., 2012, 2013; Engel and Rhoads, 2012, 2016, 2017), field observations of three-dimensional flow in the NBZ remain limited.

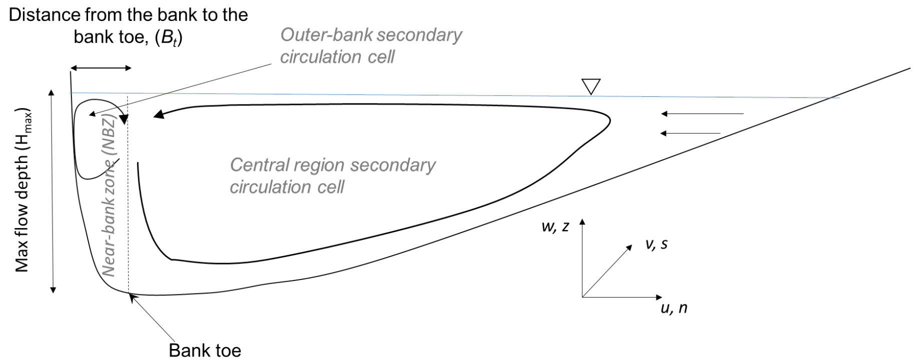

Figure 1: Definition sketch of the idealised flow components in a meander bend. Co-ordinate definitions are provided where *v*, *u* and *w* represent primary, transverse and vertical flow components of the mean cross section whilst *s*, *n* and *z*, repreesnt the conversion of these respective components onto a curvilinear grid.

The development of secondary flow in meandering channels is a result of the curvature-induced imbalance between centrifugal forces operating of the flow as it passes through a curved channel, and the cross-stream water surface slope which generate a pressure gradient directed towards the inner bank (Blanckaert et al., 2013; Rozovskii, 1957). Although in larger channels the presence of secondary flow is absent due to the large channel widths which subdue the cross-stream water surface slopes (Hackney et al., 2017; McLelland et al., 1990; Parsons et al., 2007), in smaller channels secondary flow cells, have been well described (Bathurst et al., 1977; Blanckaert et al., 2013; Markham and Thorne, 1992; Thorne et al., 1985; Thorne and Hey, 1979; Thorne and Furbish, 1995). Where flow impinges on the outer bank, bank roughness may induce a reversal of the velocity gradients, generating a secondary outer-bank cell (SOC; Figure 1) which rotates with a counter-helicity to the secondary flow cell in the channel centre. However, direct field-based quantification of the velocity profiles and turbulent structures close to outer-bends are limited in the literature. Previous field studies have assessed velocity and turbulence characteristics in the NBZ at singular discharges (Anwar, 1986; Engel and Rhoads, 2017) or has been limited to regions away from the NBZ (e.g. Sukhodolov, 2012). These studies show that turbulent kinetic energy is relatively high in the NBZ as the high-velocity core is displaced towards the bank toe. However, given the few studies which assess flow fields at a range of discharges, our understanding of the development of SOCs and their impact on turbulent kinetic energy as flow discharge varies is lacking.

Understanding is further complicated by conflicting evidence from numerical and physical experimental studies. Work by Blanckaert and Graf (2001) and Blanckaert et al. (2012) suggests that the intensity of turbulence, turbulent kinetic energy and the magnitude of Reynolds shear stressess at the outer bank are relatively low compared with the centre of the channel. These low levels of turbulence have been attribtued to the development of weak SOCs (Engel and Rhoads, 2017). Conversely, further work has demonstrated that increases in outer bank turbulence relative to the central channel flow are observed when mobile beds are present (Abad and Garcia, 2009a,b; Jamieson et al., 2010). Indeed, Sukhodolov (2012) demonstrates increased turbulent kinetic engery magnitudes with the presence of a SOC, in contradiction to the findings of Blanckaert et al. (2012). However, many of these studies were only undertaken at one flow dischange and changes in these relationshsips with flow discharge is a notable gap in understanding.

Here, we report and detail the high-resolution three-dimensional flow fields in the NBZ captured over a range of discharges (at 6 $m^3 s^{-1}$, 23 $m^3 s^{-1}$ and 90 $m^3 s^{-1}$) from a lowland meandering river in the United Kingdom. These datasets allow us to examine the role that time-averaged and turbulent near-bank flow structures play in driving turbulent kinetic energy and shear stresses in the NBZ as discharge level varies. We use this data to critically assess how the presence and development of secondary outer-bank flow cells impact the turbulent stresses directed towards the outer-bank of the channel under varying flow conditions and assess the implications of these changes for longer-term bend morphodynamics.

2. Study site and methods

Field measurements of the three-dimensional flow structure in the near bank zone were collected from a meandering reach of the River Severn, UK (Figure 2). Here, the River Severn displays alternating vertical sandy cut-banks and despite displaying classic meandering sequences incised into poorly indurated terrace gravels (Carling, 1991; Dury, 1983). The study reach has a bankfull width of 45 m and a bankfull depth of 4.3 m. Observations of flow were made at three flow discharges representing low (Q = 6 m^3 s^{-1}; August 2018), mid-flow (Q = 23 m^3 s^{-1}; January 2017) and bankfull flow conditions (Q = 90 m^3 s^{-1}; March 2017).

Detailed three-dimensional, time-mean flow velocity fields were collected using a Sontek M9 Acoustic Doppler Current Profiler (ADCP). A series of flow-perpendicular cross-sections were recorded and recaptured during each survey period (Figure 2). Each transect was surveys at least four times in order to resolve the time-averaged flow field (Szupiany et al., 2007). The ADCP was coupled with a RTK dGPS used to provide real-time positional corrections. A standard moving-platform setup was used and data was collected with multiple acoustic frequencies (1 MHz and 3 MHz) to best account for changing water level depths and speeds across the section. As such, measured cell sizes ranged from 0.06 m (1 MHz readings) to 0.1 m (3 MHz readings). The ADCP data were subsequently processed in RiverSurveyor Live and the Velocity Mapping Toolbox (VMT; Parsons et al., 2013). The resultant mean transects were then rotated using the method of Rozovskii (1957) that has been shown to capture well details of the primary and secondary flow fields in a range of complex channel planforms (Hackney et al., 2015; Lane et al., 2000; Rhoads and Kenworthy, 1995; Szupiany et al., 2009).

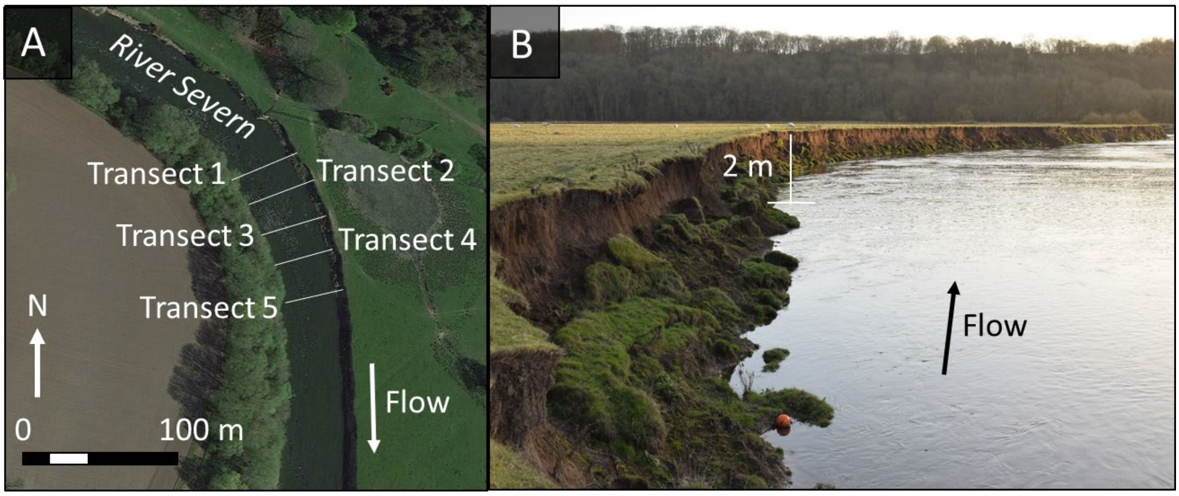

Figure 2: A) Location of the five transects covered in the study on the River Severn at Leighton, Shropshire, UK. **B)** Image of the outer bank of the reach. Note the blocks of failed material at the toe of the bank which measure ~1 m x 0.5 m x 0.3 m (L x W x D). Image taken in January 2017, when discharge was 23 $m^3 s^{-1}$. Water depths are 2 m and bank heights are ~ 2 m above the water's surface.

3. Results

3.1. Time-averaged flow

Time-averaged flow fields at each of the five transects, across the three flow discharges, reveal that a core of higher-velocity is observed in the middle of the channel away from the outer bank (Figures 3, 4 and 5). During low flow (Q = 6 $m^3 s^{-1}$; Figure 3), depth-averaged velocities range from 0.34 – 0.49 $m^3 s^{-1}$ (Table

1). Fastest flows are observed in transects one and two, with higher velocities (~0.6 $m^3 s^{-1}$) being observed near the outer bank and in the channel centre in Transect 1 (Figure 3). Secondary outer-bank cells (SOCs) are observed Transects 1, 3 and 4 at low flow levels (Figure 3).

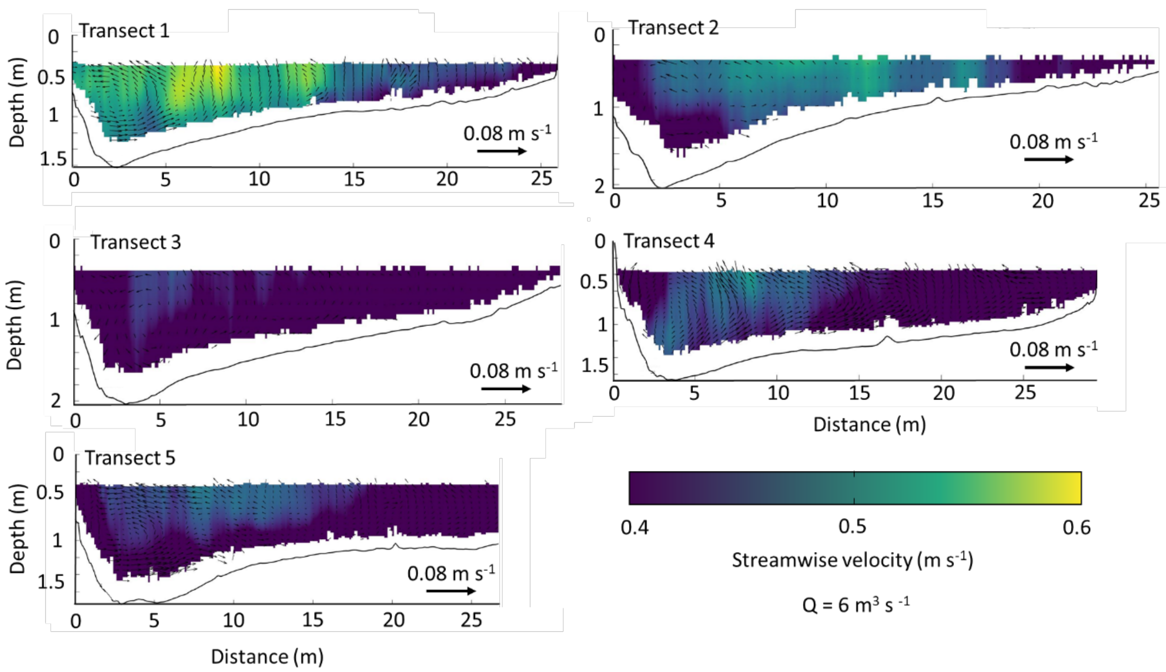

Figure 3: Streamwise flow velocities (m s^{-1}) with secondary flow vectors for each of the five transects surveyed at low flows (Q = 6 $m^3 s^{-1}$) in August 2018.

At mid-flow discharge levels (Q = 23 $m^3 s^{-1}$; Figure 4 and Table 1) depth-average velocities range from 0.64 – 0.76 $m^3 s^{-1}$ (Table 1). Flows of 0.7 m s^{-1} and greater are observed in all five transects, with high velocity cores being observed in Transects 2 – 5. In Transect 1, velocities of 0.7 m s^{-1} are observed all the way up to the outer bank (Figure 4). SOCs are observed in Transects 2 - 5, with Transect 1 displaying no SOC at this flow discharge (Figure 4).

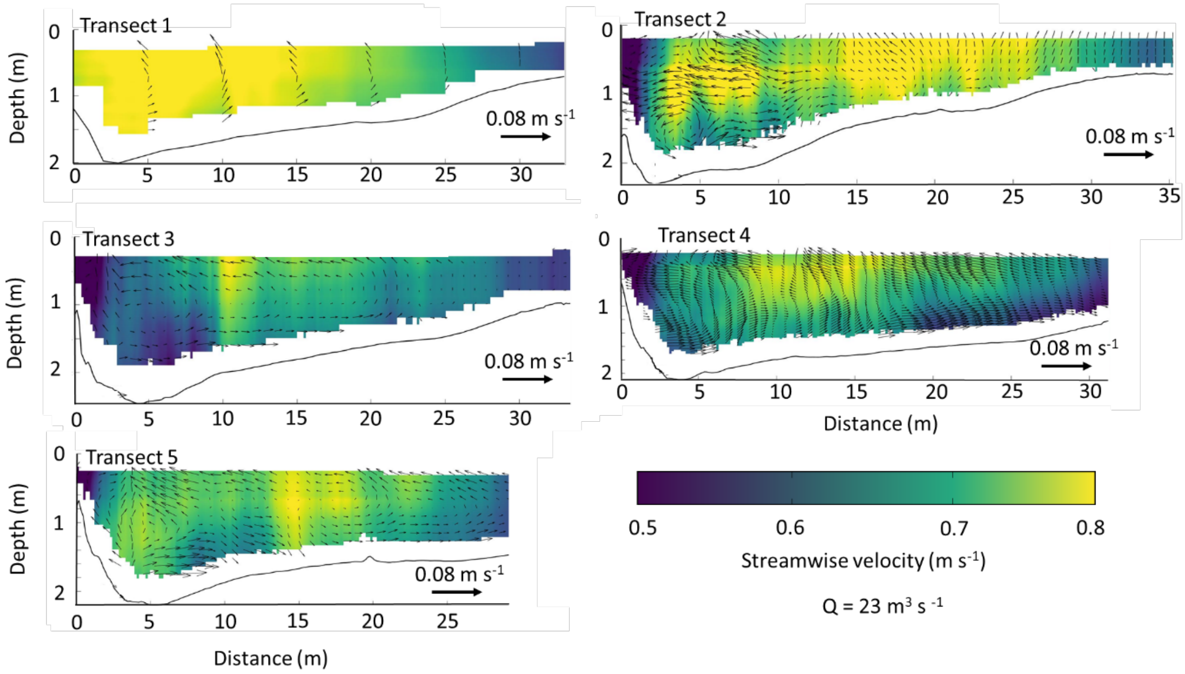

Figure 4: Streamwise flow velocities (m s^{-1}) with secondary flow vectors for each of the five transects surveyed at median flows (Q = 23 m^3 s^{-1}) in January 2017.

At bank-full flows (Q = 90 m^3 s^{-1}; Figure 5 and Table 1) depth-average velocities range from 1.08 – 1.21 m^3 s^{-1}, more than double those observed during low flow measurements (Table 1). Flows of 1.2 m s^{-1} and greater are observed in all five transects. Zones of slower flow near the outer bank are observed in Transects 1, 2 and 3, with high velocities extending to the outer bank in Transects 4 and 5. SOCs are observed in Transects 1, 3 and 4. In Transects 2 and 5 secondary flow persists up to the outer bank but appears to be one continuous secondary flow cell across the whole transect in both cases (Figure 5). In Transect 1, the SOC extends out to the bank toe; approx. 8 m from the bank edge (Figure 5). In Transect 3 the SOC extends ~ 5 m out from the bank edge, whilst in Transect 4 the SOC is reduced in width, and only extends ~2 m out from the bank edge (Figure 5).

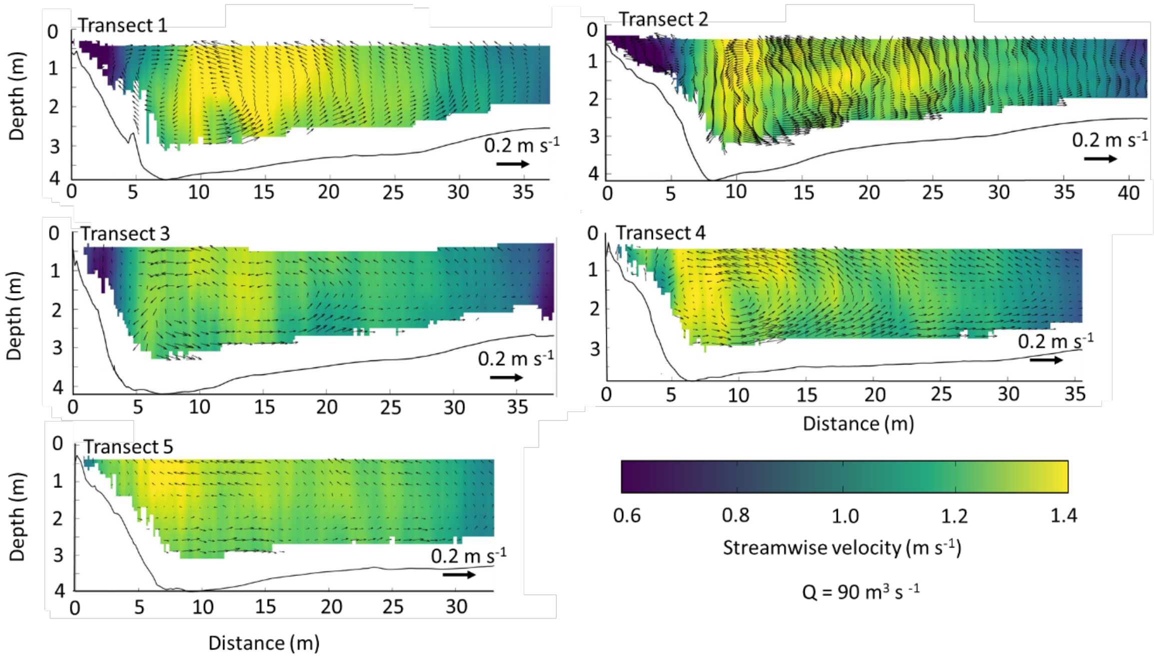

Figure 5: Streamwise flow velocities (m s^{-1}) with secondary flow vectors for each of the five transects surveyed at bankfull flows (Q = 90 m^3 s^{-1}) in March 2017*.*

Focussing in closer to the NBZ (see Figure 1 for definition), Figure 6 shows how the flow characteristics with distance from the outer bank. As can be seen, primary flow velocities increase in all transects and at all discharges with distance from the outer bank (velocity profiles in Figure 6 are plotted at 0.25B_t, 0.5B_t, 0.75B_t and 1B_t). Fully developed logarithmic flow profiles are only observed at the highest discharges and at the greatest distance from the bank edge, suggesting that the interaction between the bank and the generation of turbulent flow structures disrupts the development of velocity profiles in the NBZ. Primary flow velocities are found to be greatest in the NBZ at higher discharges. Transect 1 displays higher primary velocities in the NBZ than the other transects at low and mid-flow discharges, suggesting that the channel curvature impinges the core of high velocity upon the outer-bank at this location at these flow discharges. At higher flows, it appears the high-velocity core impinges upon the outer-bank further round the meander bend, with the highest velocities in the NBZ under high flow conditions being observed in Transects 4 and 5 (Figure 6).

TRANSECT	Q (M^3 S^{-1})	DEPTH-AVERAGED VELOCITY (M S^{-1})	MEAN FLOW DEPTH (M)	MAX FLOW DEPTH (M)
1	6	0.49	0.96	1.63
	23	0.76	1.41	2.01
	90	1.14	3.06	3.87
2	6	0.43	1.02	2.05
	23	0.72	1.41	2.30
	90	1.10	2.96	4.18
3	6	0.34	1.24	2.04
	23	0.64	1.72	2.45
	90	1.08	3.33	4.20
4	6	0.35	1.20	1.67
	23	0.66	1.66	2.10
	90	1.17	3.22	3.88
5	6	0.39	1.30	1.45
	23	0.70	1.71	2.20
	90	1.21	3.24	4.00

Table 1: Flow characteristics of the five transects at the three discharges measured.

Secondary flows are more pronounced at higher discharges in the NBZ, and are positioned further around the meander bend (Figure 6). Transitions from negative (where flow is directed away from the outer bank) to positive (where flow is directed towards the outer bank), for example observed between $0.75B_t$ and $1B_t$ at high discharges (Q = 90 m^3 s^{-1}) in Transects 3, indicate that the SOC is located between these two profiles. Similar transitions can be observed at mid-flow discharges (Q = 23 m^3 s^{-1}) in Transect 1 between $0.5B_t$ and $0.75B_t$ (Figure 6).

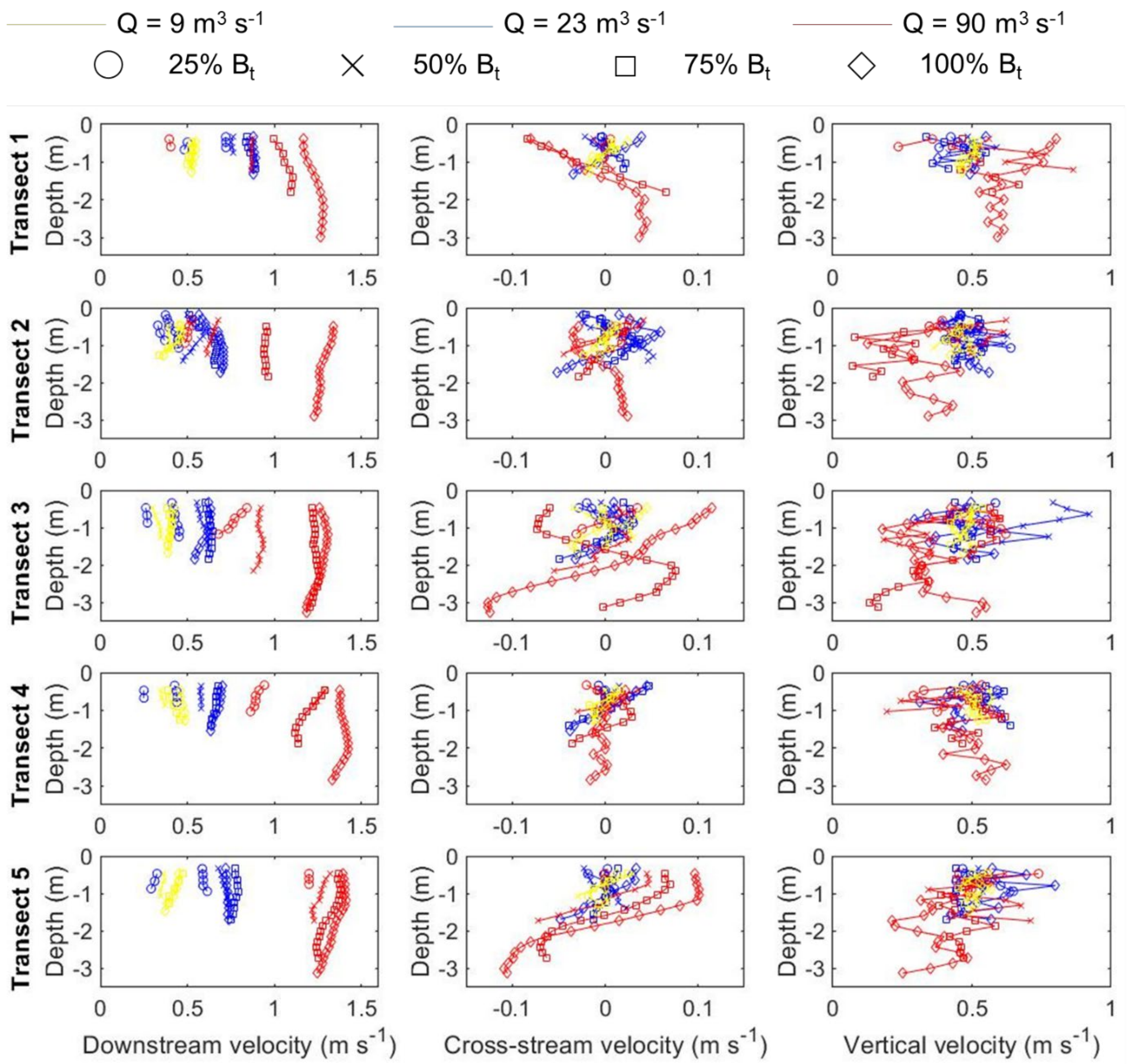

Figure 6: Near-bank downstream, cross-stream and vertical flow velocities (m s^{-1}) at the five survey transects (see Figure 1 for locations) for low flows (yellow lines, Q = 9 m^3 s^{-1}), mid-flow (blue lines, Q = 23 m^3 s^{-1}) and bank full flows (red lines, Q = 90 m^3 s^{-1}). Profiles are extracted at a range of distances from the bank to the bank toe (circles = 25% distance to bank toe, crosses = 50% distance to bank toe, squares = 75% distance to bank toes, diamonds = 100% distance to bank toe), where the bank toe is defined as the maximum channel depth around the outer bend.

3.2 Turbulence and Reynolds shear stresses

To assess the role that the SOC plays in driving turbulence and shear stresses on the near-bank and bank-toe region we define the dimensionless strength of the secondary flow component relative to the primary flow velocity, U_{s*}, following Blanckaert (2009) such that:

$$U_{s*} = \sqrt{\langle (v_n - u_n)^2 \rangle}/U \tag{1}$$

Where $(v_n - u_n)$ is the depth-averaged transverse velocity (m s^{-1}) component of the curvature-induced secondary flow and U is the depth-averaged velocity (m s^{-1}). As shown in Figure 7 secondary flow components are strong in the NBZ. At low flows (Q = 9 m^3 s^{-1}) secondary flow strength is high in Transects 1 – 3 (U_{s*} = 0.3 – 0.4), suggesting that although discharges are low, there are strong secondary flow patterns in the near bank zone, consistent with the SOCs observed in these transects at this discharge (see Figure 3). As U_{s*} drops towards the centre of the channel at this lower discharge, it is likely that the SOC is relatively stronger than the central secondary flow cell. During mid-flow conditions (Q = 23 m^3 s^{-1}), high secondary flow strength (U_{s*} =0.4) is observed in Transect 1 despite no SOC being observed in the velocity fields (see Figure 4). In the remaining four transects at these mid-flow discharges, secondary flow strength remains relatively consistent (U_{s*} = 0.1 – 0.2) often increasing towards the centre of the channel (e.g. in Transects 1 and 3) suggesting that the SOC is weaker than the central secondary cell at these discharges. At high discharge (Q = 90 m^3 s^{-1}) U_{s*} is relatively consistent across the region (~ 0.2) with some localised variation in Transect 2 and higher values (~ 0.3) observed near bank in Transect 5 (Figure 6). This suggests a relative balance between the SOC and the central secondary flow cell at this discharge.

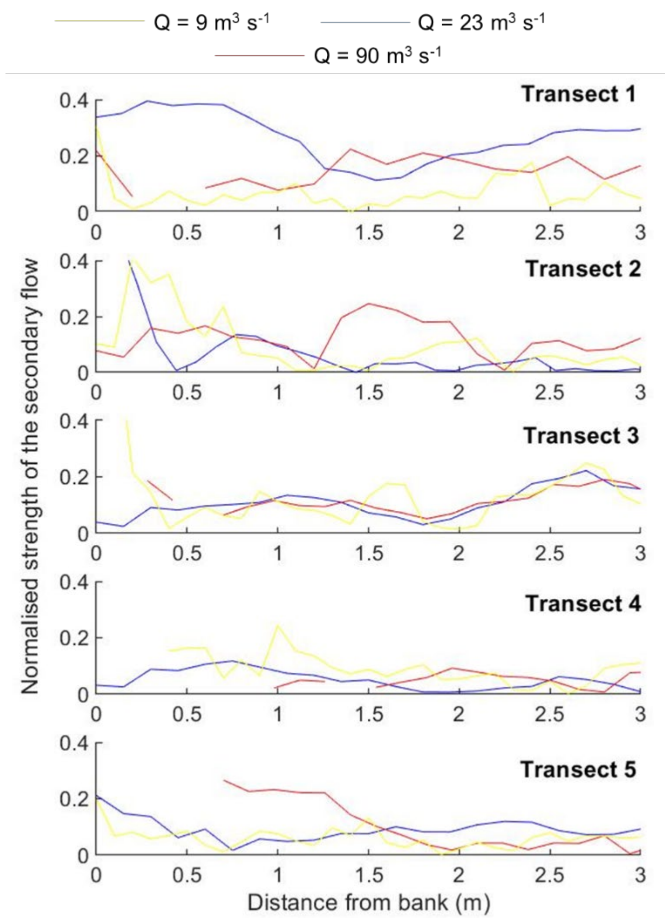

Figure 7: Near-bank distribution of the normalised strength of the secondary flow for the five surveyed transects at Q = 9 m^3 s^{-1} (yellow), Q = 23 m^3 s^{-1} (blue) and Q = 90 m^3 s^{-1} (red).

Instantaneous velocities u_i *(i = s, n, z)* from each transect were Reynolds decomposed into mean $\overline{u_i}$ $(i = s, n, z)$ and turbulent $u_i'(i = s, n, z)$ components. The turbulent kinetic energy, k, is thus calculated:

$$k = \frac{1}{2}(\overline{u_s'^2} + \overline{u_n'^2} + \overline{u_z'^2})$$

and Reynolds shear stresses, τ, are calculated as:

$$\tau_{i,j} = \overline{u_i' u_j'} \; i, j = s, n, z$$

Where *i,j* are index variables indicating the direction component of the velocities (following Engel and Rhoads, 2017). Below, the discussion focusses on the components *s* and *n* of the Reynolds shear stresses.

Turbulent kinetic energy, *k,* is greater at higher discharges in all transects (Figure 8). Magnitudes of *k* vary with distance from the bank. At low discharges (Q = 9 m^3 s^{-1}) magnitudes of *k* decrease as the distance to the bank toe increases (Figure 8). In Transect 1, depth-averaged *k* decreases from 0.4 m s^{-1} at 0.25Bt to 0.19 m s^{-1} at 1B_t. At Transect 2, depth-averaged *k* decreases from 0.25 m s^{-1} at 0.25Bt to 0.15 m s^{-1} at 0.7B_t, although rises again at 1Bt to 0.23. At Transect 3, depth-averaged *k* increases from 0.16 at 0.25B_t to 0.29 at 0.75B_t before decreasing to 0.19 at 1B_t. At Transect 4, depth-averaged *k* increases from 0.12 at 0.25B_t to 0.18 at 0.5B_t before decreasing to 0.15 at 1B_t. At Transect 5, depth-averaged *k* decreases from 0.28 at 0.25B_t to 0.18 at 1B_t.

At mid-flow (Q = 23 m^3 s^{-1}) in Transect 1, depth-averaged *k* increases from 0.66 m s^{-1} at 0.25Bt to 0.85 m s^{-1} at 1B_t (Figure 8). At Transect 2, depth-averaged *k* remains consistent at 0.44 m s^{-1}, only varying by 0.05 m s^{-1} between 0.25Bt and 1Bt. At Transect 3, depth-averaged *k* decreases from 0.47 at 0.25B_t to 0.3 at 1B_t. At Transects 4 and 5, depth-averaged *k* remain consistently at around 0.3 m s^{-1} ± 0.05 m s^{-1} at all distances from the bank toe.

At high discharges (Q = 90 m^3 s^{-1}) the highest values of *k* are observed, with some locations seeing 0.9 m s^{-1} (Figure 8). In Transect 1, depth-averaged *k* increases from 0.38 m s^{-1} at 0.25Bt to 0.88 m s^{-1} at 0.75B_t before decreasing to 0.7 m s^{-1} at 1B_t (Figure 8). At Transect 2, depth-averaged *k* increases at 0.35 m s^{-1} at 0.25B_t to 0.47 at 1Bt. At Transect 3, depth-averaged *k* increases from 0.46 at 0.25B_t to 0.6 at 1B_t. At Transects 4, depth-averaged *k* decreases from 0.86 m s^{-1} at 0.25B_t to 0.58 at 1B_t. Similarly, at Transect 5, depth-averaged k decreases from a peak value of 0.9 m s^{-1} at 0.25B_t to 0.35 m s^{-1} at 1B_t (Figure 8).

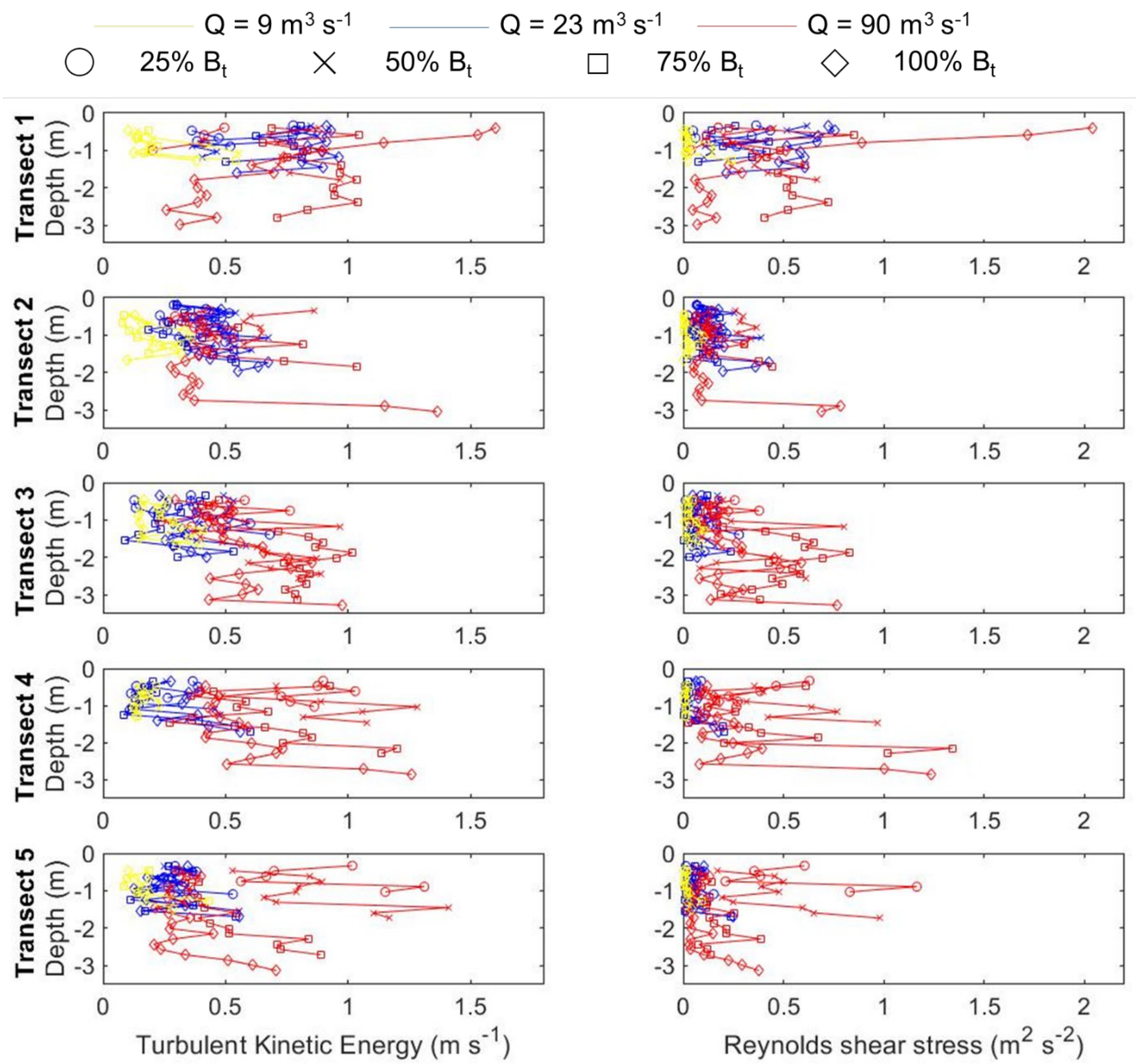

Figure 8: Near-bank turbulent kinetic energy (m s^{-1}) and Reynolds shear stresses (m^2 s^{-2}) at the five survey transects (see Figure 1 for locations) for low flows (yellow lines, Q = 9 m^3 s^{-1}), mid-flow (blue lines, Q = 23 m^3 s^{-1}) and bank full flows (red lines, Q = 90 m^3 s^{-1}). Profiles are extracted at a range of distances from the bank to the bank toe (circles = 25% distance to bank toe, crosses = 50% distance to bank toe, squares = 75% distance to bank toes, diamonds = 100% distance to bank toe), where the bank toe is defined as the maximum channel depth around the outer bend.

Reynolds shear stresses, τ, are greater at higher discharges in all transects (Figure 8). At low discharges (Q = 9 m^3 s^{-1}) magnitudes of τ increase as the distance to the bank toe increases (Figure 8), but decrease around the meander bend, with shear stresses in Transect 1 being relatively greater (depth-average τ = 0.06 m^2 s^{-2}) than those observed in Transect 5 (depth-average τ = 0.03 m^2 s^{-2}). All five transects show peak τ values close to the bed, with τ increasing with depth. In Transect 1, peak τ values (τ = 0.24 m^2 s^{-2}) are observed at $0.75B_t$ at the bed. Higher up in the vertical profile, τ is consistent at 0.02 – 0.03 m^2 s^{-2} at all distances from the bank. At the bank toe ($1B_t$) τ is consistently at 0.01 m^2 s^{-2}, displaying a marked reduction in magnitudes from those observed at $0.75B_t$.

At mid-flow discharges (Q = 23 m^3 s^{-1}) magnitudes of τ again increase as the distance to the bank toe increases (Figure 8), but decrease around the meander bend, with shear stresses in Transect 1 being greater (depth-average τ = 0.38m^2 s^{-2}) than those observed in Transect 5 (depth-average τ = 0.07 m^2 s^{-2}). Transects 2 - 5 show peak τ values close to the bed, with τ increasing with depth (Figure 8). However, in Transect 1 peak τ are observed close to the water's surface, and decrease towards the bed. In Transect 1, peak τ values (τ = 0.75 m^2 s^{-2}) are observed at $0.1B_t$ at the water's surface, with values decreasing to 0.22 m^2 s^{-2} at the bed. In transects 3-5 τ ranges from 0.05 – 0.2 m^2 s^{-2} consistently with higher values present at the bed and at greater distances from the river bank.

At high discharges (Q = 90 m^3 s^{-1}) magnitudes of τ are more consistent throughout the five transects, with no discernible decrease around the meander bend (Figure 8) observable. Values are also higher than those recorded at low and mid-flows. Values of τ at all transects increase towards the bed. τ is greatest at $0.75B_t$ in Transect 1 (depth-averaged τ = 0.5 m^2 s^{-2}), although maximum τ values at Transect 1 are observed at $1B_t$ at the water's surface (τ = 1.6 m^2 s^{-2}). In Transect 5 the highest τ values are observed at $0.25B_t$ and $0.5B_t$ (depth-averaged τ = 0.59 m^2 s^{-2} and 0.47 m^2 s^{-2}, respectively), with values further away from the bank considerably smaller ($0.75B_t$ τ = 0.15 m^2 s^{-2} and $1B_t$ τ = 0.09 m^2 s^{-2}).

Discussion

Our results demonstrate that the patterns and magnitudes of turbulent flows, Reynold shear stresses and the development of secondary outer-bank cells (SOCs) change as discharge levels vary in a meander bend. We observe that the magnitudes of all quantities increase as flow discharge increases. However, spatial variations between locations around the meander bend are subdued as flow discharges increase, resulting in more uniform flow dynamics throughout the reach. At low flows the most upstream bend transects, Transects 1 and 2, show a high relative strength of the secondary flow components (Figure 7) when compared the three downstream transects. However, as discharges increase, the relative strength of the near-bank secondary flow strength become closer in magnitude. In fact at the highest discharges the furthest downstream transect, Transect 5, displays the greatest normalised secondary flow strength (Figure 7).

This pattern is also reflected in the location of the high velocity flow core (Figures 3, 4 and 5). Engel and Rhoads (2017) propose a conceptual model of the velocity distribution (henceforth termed the ER17 model), and related turbulence and shear stresses, through a meander bend based on results from a single flow discharge. In the ER17 model the high velocity core progressively moves towards the outer-bank and the bank toe through the meander. Our results support this model for high discharges, where increased primary velocities are observed close to the bank toe at the downstream extent of the meander bend (Figure 6). However, at mid- and lower flow discharges, the fastest flows near the outer bank were observed at the upstream extent of the meander bend (Figure 6), where the highest secondary flow strength was also observed (Figure 7). Given the ER17 model was also developed on data collected at mid-flow conditions (Engel and Rhoads, 2017), this discrepancy is likely due to the higher curvature of the meander bend in which data underpinning the ER17 model was collected. Our results suggest for lower curvature bends the ER17 model may only be appropriate at higher discharges, and that at low and mid-flow levels where the high velocity cells tends to be shifted away from the outer bank through the bend and the SOC strength is supressed (Figure 6), the ER17 model breaks down.

The deflection of the higher velocity flow cell at low and mid-flows may be a result of the presence of failed material at the bank toe (Hackney et al., 2015; Parker et al., 2011; Wood et al., 2008; Figure 1B). The ER17 model depicts this deflection in its final stage, showing the high velocity core moving back towards the channel centre. It is possible that for our low and mid-flow data, slump blocks at the bank toe are a primary control on the flow in the NBZ, whilst at high discharges their influence is subsumed by the high flow levels, and their submergence alters the direction of their influence, deflecting flow up and onto the outer bank (Hackney et al., 2015).

We also observe that when SOCs are present at high discharges (in Transects 1, 3 and 4), TKE values are also typically higher than in transects where no SOCs are observed (Figure 8). This pattern is reversed at mid-flows where the presence of SOCs (in Transects 2, 3, 4 and 5) are associated with lower values of TKE than in Transect 1 where no SOC is present (Figure 8). At low flows TKE values are consistent throughout each transect regardless of the presence of SOCs. This again shows a clear and critical dependence on discharge levels. Prior work has demonstrated that the presence of SOCs can increase turbulence levels (Sukhodolov, 2012), whilst experimental work (Blanckaert et al., 2012) suggests that SOCs are associated with reduced TKE. Both Sukhodolov (2012) and Blanckaert et al. (2012) report observations in bends at a single discharge. In comparison, our results across a range of discharges suggest that the relationship between TKE and the presence of SOCs is discharge dependent, and thus more nuanced than single-discharge studies have previously reported. This has a range of implications for bank erosion processes through relative controls on the distributions of the greatest magnitudes of outer bank shear.

Conclusion

This paper reports observations of three-dimensional flow characteristics in the near-bank zone of a meander bend at a range of discharge levels; low (9 $m^3 s^{-1}$), mid- (23 $m^3 s^{-1}$) and bankfull (90 $m^3 s^{-1}$). Through the application of high-resolution ADCP data primary and secondary flow structures were described and characteristics of turbulent kinetic energy (TKE) and Reynolds shear stresses were decomposed. Our results reveal that the relationship between the presence of a secondary outer-bank flow cell (SOC) and magnitudes of TKE and shear stresses vary with discharge. At high flows, the presence of a SOC is related to increased TKE, whilst at mid-flow discharges SOCs are associated with reduced TKE compared to transects where SOCs are absent. At low flows there is no observed pattern between TKE and the presence/absence of a SOC. We attribute these patterns to the role that failed material at the bank toe plays in deflecting and modulating near-bank flows. This work highlights how important detailed flow data across multiple discharges is in terms of understanding flow through meander bends and thus the impact these flow processes will have on longer term bend morphodynamics.

Acknowledgements

CRH acknowledges an Early Career Researcher grant from the British Society for Geomorphology which funded this work. Thanks are also expressed to Hao Hu, Leiping Ye and Annie Ockelford for help in the field data collection. DP acknowledges funding by the European Research Council for the programme GEOSTICK (Grant agreement ID: 725955)

Data availability statement

All data will be made available on request to the corresponding author.

Conflict of interest disclosure

The authors declare no conflicts of interest.

References

Abad JD, Garcia MH. 2009a. Experiments in a high-amplitude Kinoshita meandering channel: 1. Implications of bend orientation on mean and turbulent flow structure. Water Resources Research **45** DOI: 10.1029/2008WR007016 [online] Available from: http://doi.wiley.com/10.1029/2008WR007016

(Accessed 26 July 2017)

Abad JD, Garcia MH. 2009b. Experiments in a high-amplitude Kinoshita meandering channel: 2. Implications of bend orientation on bed morphodynamics. Water Resources Research **45** DOI: 10.1029/2008WR007017 [online] Available from: http://doi.wiley.com/10.1029/2008WR007017 (Accessed 26 July 2017)

Anwar HO. 1986. Turbulent structures in a river bend. Journal of Hydraulic Engineering1y **112** : 657–669.

Bathurst JC, Thorne CR, Hey RD. 1977. Direct measurement of secondary currents in river bends. Nature **269** : 504–506.

Blanckaert K. 2009. Saturation of curvature-induced secondary flow, energy losses, and turbulence in sharp open-channel bends: Laboratory experiments, analysis, and modeling. Journal of Geophysical Research **114** DOI: 10.1029/2008JF001137 [online] Available from: http://doi.wiley.com/10.1029/2008JF001137 (Accessed 13 August 2014)

Blanckaert K, Duarte A, Chen Q, Schleiss AJ. 2012. Flow processes near smooth and rough (concave) outer banks in curved open channels. Journal of Geophysical Research **117** : F04020. DOI: 10.1029/2012JF002414 [online] Available from: http://doi.wiley.com/10.1029/2012JF002414 (Accessed 13 June 2013)

Blanckaert K, Graf WH. 2001. Mean Flow and Turbulence in Open-Channel Bend. Journal of Hydraulic Engineering **127** : 835–847. DOI: 10.1061/(ASCE)0733-9429(2001)127:10(835) [online] Available from: http://ascelibrary.org/doi/10.1061/%28ASCE%290733-

9429%282001%29127%3A10%28835%29 (Accessed 26 July 2017)

Blanckaert K, Kleinhans MG, McLelland SJ, Uijttewaal WSJ, Murphy BJ, van de Kruijs A, Parsons DR, Chen Q. 2013. Flow separation at the inner (convex) and outer (concave) banks of constant-width and widening open-channel bends. Earth Surface Processes and Landforms **38** : 696–716. DOI: 10.1002/esp.3324 [online] Available from: http://doi.wiley.com/10.1002/esp.3324 (Accessed 26 July 2017)

Brice JC. 1974. Evolution of meander loops. Geological Society of America Bulletin **85** : 581–586.

Carling PA. 1991. An appraisal of the velocity-reversal hypothesis for stable pool-riffle sequences in the river severn, England. Earth Surface Processes and Landforms **16** : 19–31. DOI: 10.1002/ESP.3290160104

Dury GH. 1983. Osage-type underfitness to the River Severn near Shrewsbury, Shropshire, England. In Background to Palaeohydrology , Gregory KJ (ed). Wiley: Chichester; 399–412.

Engel FL, Rhoads BL. 2012. Interaction among mean flow, turbulence, bed morphology, bank failures and channel planform in an evolving compound meander loop. Geomorphology **163–164** : 70–83. DOI: 10.1016/j.geomorph.2011.05.026 [online] Available from: http://linkinghub.elsevier.com/retrieve/pii/S0169555X11003886 (Accessed 26 July 2017)

Engel FL, Rhoads BL. 2016. Three-dimensional flow structure and patterns of bed shear stress in an evolving compound meander bend. Earth Surface Processes and Landforms **41** : 1211–1226. DOI: 10.1002/esp.3895 [online]

Available from: http://doi.wiley.com/10.1002/esp.3895 (Accessed 26 July 2017)

Engel FL, Rhoads BL. 2017. Velocity profiles and the structure of turbulence at the outer bank of a compound meander bend. Geomorphology **295** : 191–201. DOI: 10.1016/j.geomorph.2017.06.018 [online] Available from: http://linkinghub.elsevier.com/retrieve/pii/S0169555X17302805 (Accessed 26 July 2017)

Hackney CR, Best JL, Leyland J, Darby SE, Parsons DR, Aalto RA, Nicholas AP. 2015. Modulation of outer bank erosion by slump blocks: Disentangling the protective and destructive role of failed material on the three-dimensional flow structure. Geophysical Research Letters **42** : 10633–10677. DOI: 10.1002/2015GL066481.Received [online] Available from: http://doi.wiley.com/10.1002/2015GL066481 (Accessed 2 December 2015)

Hackney CR, Darby SE, Parsons DR, Leyland J, Aalto R, Nicholas AP, Best JL. 2017. The influence of flow discharge variations on the morphodynamics of a diffluence-confluence unit on a large river. Earth Surface Processes and Landforms DOI: 10.1002/esp.4204 [online] Available from: http://doi.wiley.com/10.1002/esp.4204

Jamieson EC, Post G, Rennie CD. 2010. Spatial variability of three-dimensional Reynolds stresses in a developing channel bend. Earth Surface Processes and Landforms **35** : 1029–1043. DOI: 10.1002/esp.1930 [online] Available from: http://doi.wiley.com/10.1002/esp.1930 (Accessed 26 July 2017)

Kean JW, Smith JD. 2006a. Form drag in rivers due to small-scale natural topographic features: 1. Regular sequences. Journal of Geophysical Research **111** : F04009. DOI: 10.1029/2006JF000467 [online] Available from: http://doi.wiley.com/10.1029/2006JF000467 (Accessed 19 June 2013)

Kean JW, Smith JD. 2006b. Form drag in rivers due to small-scale natural topographic features: 2. Irregular sequences. Journal of Geophysical Research **111** : F04010. DOI: 10.1029/2006JF000490 [online] Available from: http://doi.wiley.com/10.1029/2006JF000490 (Accessed 19 June 2013)

Konsoer K, Rhoads B, Best J, Langendoen E, Ursic M, Abad J, Garcia M. 2017. Length scales and statistical characteristics of outer bank roughness for large elongate meander bends: The influence of bank material properties, floodplain vegetation and flow inundation. DOI: 10.1002/esp.4169

Konsoer KM, Rhoads BL, Langendoen EJ, Best JL, Ursic ME, Abad JD, Garcia MH. 2016. Spatial variability in bank resistance to erosion on a large meandering, mixed bedrock-alluvial river. Geomorphology **252** : 80–97. DOI: 10.1016/j.geomorph.2015.08.002 [online] Available from: http://dx.doi.org/10.1016/j.geomorph.2015.08.002

Lane SN, Bradbrook KF, Richards KS, Biron PM, Roy AG. 2000. Secondary circulation cells in river channel confluences : measurement artefacts or coherent flow structures ? Hydrological Processes **14** : 2047–2071.

Markham AJ, Thorne CR. 1992. Geomorphology of gravel-bed river bends. In Dynamics of Gravel-Bed Rivers , Billi P, Hey RD, Thorne CR, and Tacconi P (eds). Wiley: Chichester; 433–457.

McLelland SJ, Ashworth PJ, Best JL, Roden J, Klaassen GJ. 1990. Flow structure and transport of sand-grade suspended sediment around an evolving braid bar, Jamuna River, Bangladesh. Special Publication of the International Association of Sedimentologists **28** : 43–57. DOI: 10.1002/9781444304213.ch4

Parker G, Shimizu Y, Wilkerson G V., Eke EC, Abad JD, Lauer JW, Paola C, Dietrich WE, Voller VR. 2011. A new framework for modeling the migration of meandering rivers. Earth Surface Processes and Landforms **36** : 70–86. DOI: 10.1002/esp.2113 [online] Available from: http://doi.wiley.com/10.1002/esp.2113 (Accessed 30 July 2014)

Parsons DR, Best JL, Lane SN, Orfeo O, Hardy RJ, Kostaschuk R. 2007. Form roughness and the absence of secondary flow in a large confluence–diffluence, Rio Paraná, Argentina. Earth Surface Processes and Landforms **32** : 155–162. DOI: 10.1002/esp.1457 [online] Available from: http://doi.wiley.com/10.1002/esp.1457 (Accessed 30 May 2013)

Parsons DRR, Jackson PRR, Czuba JAA, Engel FLL, Rhoads BLL, Oberg KA, Best JLL, Mueller DSS, Johnson KKK, Riley JDD. 2013. Velocity Mapping Toolbox (VMT): a processing and visualization suite for moving-vessel ADCP measurements. Earth Surface Processes and Landforms **38** : 1244–1260. DOI: 10.1002/esp.3367 [online] Available from: http://doi.wiley.com/10.1002/esp.3367 (Accessed 20 June 2013)

Rhoads BL, Kenworthy ST. 1995. Flow structure at an asymmetrical stream confluence. Geomorphology **11** : 273–293. DOI: 10.1016/0169-555X(94)00069-4 [online] Available from: http://linkinghub.elsevier.com/retrieve/pii/0169555X94000694

Rinaldi M, Darby SE. 2007. Modelling river bank erosion processes and mass failure mechanisms: Progress towards fully coupled simlations. In Gravel Bed Rivers VI: Form Process Understanding to River Restoration , Habersack H, Piégay H, and Rinaldi M (eds). Elsevier: Amsterdam; 213–239.

Rozovskii IL. 1957. Flow of water in bends of open channels. Akad. Sci. Ukrainian SRR

Sukhodolov AN. 2012. Structure of turbulent flow in a meander bend of a lowland river. Water Resources Research **48** DOI: 10.1029/2011WR010765 [online] Available from: http://www.agu.org/pubs/crossref/2012/2011WR010765.shtml (Accessed 20 June 2014)

Szupiany RN, Amsler ML, Best JL, Parsons DR. 2007. Comparison of Fixed- and Moving-Vessel Flow Measurements with an aDp in a Large River. Journal of Hydrologic Engineering **133** : 1299–1309. DOI: 10.1061/(ASCE)0733-9429(2007)133:12(1299)

Szupiany RN, Amsler ML, Parsons DR, Best JL. 2009. Morphology, flow structure, and suspended bed sediment transport at two large braid-bar confluences. Water Resources Research **45** : n/a-n/a. DOI: 10.1029/2008WR007428 [online] Available from: http://doi.wiley.com/10.1029/2008WR007428 (Accessed 4 October 2013)

Thorne CR, Hey RD. 1979. Direct measurements of secondary currents at a river inflexion point. Nature **280** : 226–228.

Thorne CR, Zevenbergen LW, Pitlick JC, Rais S, Bradley JB, Julien PY. 1985. Direct measurements of secondary currents in a meandering sand-bed river. Nature **315** : 746–747.

Thorne SD, Furbish JD. 1995. Influences of coarse bank roughness on flow within a sharply curved fiver bend. Geomorphology **12** : 241–257.

Wood SH, Ziegler AD, Bundarnsin T. 2008. Floodplain deposits, channel changes and riverbank stratigraphy of the Mekong River area at the 14th-Century city of Chiang Saen, Northern Thailand. Geomorphology **101** : 510–523. DOI:

10.1016/j.geomorph.2007.04.030 [online] Available from: http://linkinghub.elsevier.com/retrieve/pii/S0169555X08000718 (Accessed 4 June 2013)